physica status solidi

pss

www.pss-journals.com

reprint

WILEY-VCH

Phys. Status Solidi A **212**, No. 9, 1888–1896 (2015) / **DOI** 10.1002/pssa.201532006

physica status solidi a
www.pss-a.com
applications and materials science

Microstructural evolution of a recrystallized Fe-implanted InGaAsP/InP heterostructure

André Fekecs[1], Andreas Korinek[2], Martin Chicoine[3,4], Bouraoui Ilahi[,1], François Schiettekatte[3,4], Denis Morris[1,4], and Richard Arès[*,1,4]**

[1] Institut Interdisciplinaire d'Innovation Technologique (3IT), and Laboratoire Nanotechnologies Nanosystèmes (LN2)-CNRS UMI-3463, Université de Sherbrooke, 3000 boul. de l'Université, Sherbrooke, QC, Canada J1K OA5
[2] Department of Materials Science and Engineering, and Canadian Centre for Electron Microscopy, McMaster University, 1280 Main Street West, Hamilton, ON, Canada L8S 4M1
[3] Département de Physique, Université de Montréal, C.P. 6128, Succursale Centre-Ville, Montréal, QC, Canada H3C 3J7
[4] Regroupement Québécois sur les Matériaux de Pointe (RQMP), QC, Canada

Received 29 November 2014, revised 2 March 2015, accepted 2 March 2015

Keywords heterostructures, InGaAsP, ion implantation, recrystallization, transmission electron microscopy, X-ray diffraction

---

[*] Corresponding author: e-mail richard.ares@usherbrooke.ca, Phone: 1 819 821 8000 ext. 65012, Fax: 1 819 821 7937
[**] Present address: Department of Physics and Astronomy, King Saud University, P.O. Box 2455, Riyadh 11451, Saudi Arabia.

Through the recrystallization of an amorphous heterostructure, obtained by MeV Fe ion implantation, we are able to tailor a standard epitaxial semiconductor material, a small gap InGaAsP/InP alloy, for photoconductive terahertz optoelectronics. Here, we report on microstructural changes occurring in the material over a broad range of rapid thermal annealing temperatures, using X-ray diffraction line profile analysis and transmission electron microscopy. Results show a complete amorphous transition of the heterostructure after multiple-energy implantations done at 83 K. Upon thermal annealing, multiple structural layers develop via solid phase epitaxy and solid phase recrystallization. The photoconductive InGaAsP layer becomes polycrystalline and submicron grained, with high crystalline volume fraction and apparent $\langle 110 \rangle$ texture. Many grains are elongated and internally faulted, with high densities of planar faults occurring on closed-packed (111) planes. The X-ray diffraction line broadening is anisotropic and evolves with rapid thermal annealing temperatures. At 500 °C, the X-ray coherent domain size estimate of 10 nm is aligned reasonably with electron microscopy made in faulted areas. Above 500 °C, a significant decrease of the planar fault density is detected. We discuss the influence of these microstructural changes happening with recrystallization temperatures on the ultrafast photoconductive response of Fe-implanted InGaAsP/InP.

1 Introduction Under specific processing conditions, ultrafast photoconductive properties are achieved in bulk semiconductor materials, such as ternary $In_{0.53}Ga_{0.47}As/InP$ and quaternary $In_{0.61}Ga_{0.39}As_{0.87}P_{0.13}/InP$ heterostructures, following ion implantation with Fe ions and rapid thermal annealing (RTA) [1–3]. These Fe-implanted small gap materials were developed to build photoconductive emitters and detectors for novel terahertz spectrometer systems working at 1550 nm, the operating wavelength of practical designs integrating an erbium-doped femtosecond fiber laser [3–7]. For emitter devices, broadband terahertz emission can be produced at the picosecond timescale via photo-induced conductivity transients when a region of the heterostructure, located between externally biased electrodes, is illuminated by short pulses. Achieving high dark sheet resistivity is very important for allowing substantial external bias [8]. If the resistivity of the material is too low, emitter devices may suffer from Joule heating. In particular, Joule heating is known to limit the performance of interdigitated large area devices made for 1550 nm operation [9]. When done at room temperature in $In_{0.53}Ga_{0.47}As$ materials, MeV Fe ion implantation has produced sheet resistivities of 0.24 and 0.5 MΩ/sq [1, 2]. However, with $In_{0.61}Ga_{0.39}As_{0.87}P_{0.13}/InP$ layers implanted at 83 K, we reported much higher sheet resistivity, of more than 10 MΩ/sq [3].

These "macroscopic" optoelectronic properties, i.e., dark resistivity and photocarrier decay times, are strongly influenced by the evolution of material microstructures throughout the fabrication process. Microstructural effects were thoroughly discussed for ultrafast GaAs devices made by As ion implantation by Tan and colleagues [10] who stress that different types of post-annealing defects, such as point defects, clusters, dislocation loops, or polycrystalline grain boundaries, are strongly dependent on the primary damage profile and directly influence carrier dynamics. With cold Fe-implanted InGaAsP, our previous work showed that the primary implantation damage from high Fe ion fluence is causing strong optical absorption tails beyond the original band edge wavelength of the quaternary alloy [3]. The effect is consistent with an amorphization of the InGaAsP layer, which is also predicted by the simulation of atomic displacements of the implantation damage [3]. Thermal annealing can in principle allow the recrystallization of these amorphous regions. After RTA, we have observed negligible changes in the tails of the optical absorption spectra of our implanted samples but a significant improvement of the effective Hall mobility [3]. These observations suggest a crystalline recovery taking place but leaving secondary disorder, such as a residual amorphous phase and/or structural defects into the heterostructure. Such imperfections could lead to a high density of energy-distributed traps which are believed to be responsible for the sub-picosecond photocarrier dynamics of this material [3, 11]. It is worth noticing that high defect densities, able to capture free carriers, are typically associated with high field breakdown [12]. For this material, fields up to 50 kV/cm have been applied on illuminated devices without catastrophic breakdown.

In this context, this structural study provides evidence for defective microstructures formed during the recrystallization of amorphous Fe-implanted InGaAsP/InP heterostructures. Since the photocarrier dynamics of the material slows down gradually as a function of the RTA temperature [3], we are specifically looking for RTA-dependent structural changes responsible for a possible co-existence of crystalline phases and regions containing defects acting as efficient traps. In this work, quantitative structural estimates are made based on peak analysis of powder X-ray diffraction (XRD) data. The results are correlated to electron diffraction patterns and images obtained with transmission electron microscopy (TEM). Our findings support the idea that nanoscale structural defects produced by the recrystallization process are at the origin of desirable optoelectronic properties found in cold Fe-implanted InGaAsP.

2 Experimental

2.1 Material and sample preparation Specific details on epitaxial InGaAsP/InP growth, simulation of optimized implantation and damage profiles, multiple high-energy Fe ion implantation, and on RTA were given previously [3]. They are summarized here. A sequence of not intentionally doped layers of InP (0.1 μm), $In_{0.61}Ga_{0.39}As_{0.87}P_{0.13}$ (1.5 μm), and InP (0.1 μm) were grown epitaxially on semi-insulating (001) InP substrates. The absorption band edge wavelength was 1.57 μm. These heterostructures were implanted by a five-energy Fe ion sequence (up to 2.5 MeV), which was designed to obtain uniform implantation damage and Fe incorporation into the whole InGaAsP layer. Samples were held cold, at 83 K, during the implantation, which avoided dynamical defect annealing and favored implant damage accumulation. The implantation sequence had a total ion fluence of $1.9 \times 10^{15}\,\mathrm{cm}^2$ which created, from simulations, an average of 6.5 atomic displacements per atoms, and incorporated Fe at about 0.03 at%. Next, the implanted samples were processed in a lamp-based rapid thermal annealer at various temperatures between 400 and 750 °C. The linear temperature ramp up was completed in 20 s and the RTA temperature plateau was held for 30 s. One sample was annealed at 300 °C, which corresponds to the temperature used for sintering indium contacts for about 75 s. These electrical contacts were easily scraped off before structural measurements. For many samples of this study, the thin InP cap layer was removed by means of selective chemical etching before structural measurements.

2.2 XRD measurements XRD measurements were made on an X'pert Pro MRD powder diffractometer (PANalytical) in the Bragg–Brentano geometry equipped with a Xe-filled proportional detector. The X-ray wavelength was 1.54 Å (Cu_α lines). The source divergence slit opening was set to 0.25°. The powder XRD instrument was able to detect weak signals over wide ω–2θ coupled scans (up to $2\theta = 100°$). Contrary to a high resolution XRD machine, it does not allow for fine adjustment of the tilt angle (ψ) of the sample. Therefore, symmetrical peaks signals from the InP single crystal substrate may not always give accurate intensity and width. Diffractograms were taken on samples of identical size ($6 \times 6\,\mathrm{mm}^2$). Since the implant-damaged and recrystallized layers had similar thicknesses, their diffractograms (number of counts as a function of 2θ) could be compared directly without geometrical corrections. The instrument's broadening function was determined by measuring a LaB_6 powder standard (SRM 660b) from the National Institute of Standards and Technology (NIST). Details of the peak shape analysis are given in the Supporting Information.

Using peak shape parameters, we calculated crystalline fractions X_c with the following expression: $X_c = I_c/(I_a + I_c)$, where I_c and I_a are integrated intensities of signals scattered from crystalline and amorphous phases. For the crystalline phase, three main reflections contribute to the integrated intensity ($I_c = I_{111} + I_{220} + I_{311}$). I_{hkl} also includes contributions from all subreflection assigned to planar faults (PFs). According to the InP diffraction powder standard, the summation of those three reflections accounts for 89% of the total integrated intensity up to $2\theta = 60°$; therefore, omitting

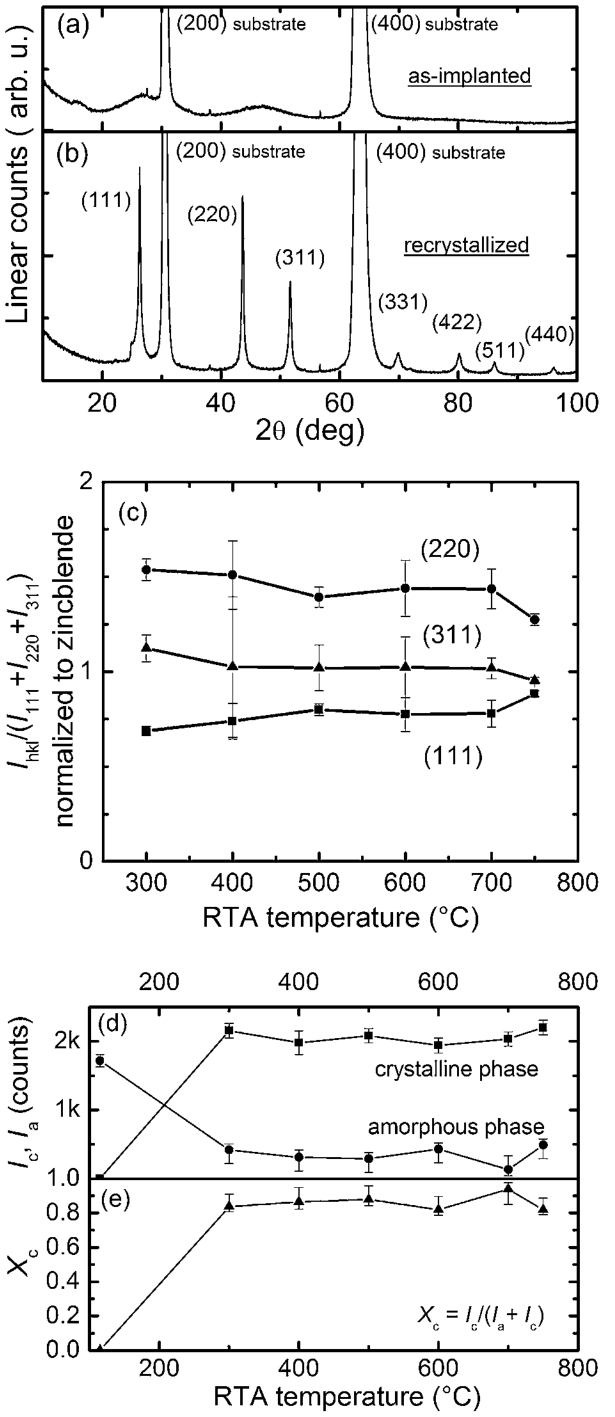

Figure 1 X-ray diffraction spectra from wide ω–2θ coupled scans of (a) Fe-implanted InGaAsP and then (b) annealed at 550 °C for 30 s. Each scan was ~10 h long for better detection of weak reflections beyond 70°. (c) Preferential orientation showing the relative contribution of each *hkl* reflection normalized to random zincblende powder standard. These values are obtained for different annealing temperatures of the recrystallized Fe-implanted InGaAsP material. (d) Peak analysis of the amorphous-to-crystalline transformation showing integrated scattered intensities of the amorphous phase I_a and the crystalline phase I_c. (e) Evolution of the crystalline volume fraction X_c.

weaker reflections in the analysis was acceptable. For the amorphous phase, the first two halos centered at 27 and 47° were summed as $I_a = I_{27°} + I_{47°}$. This approach has been applied before on microcrystalline silicon samples with XRD data taken in grazing incidence [13, 14] and in the Bragg–Brentano configuration [15]. For the analysis of texture, integrated peak intensities were compared to each other, relative to the zincblende InP powder diffraction standard (ICDD 17 04-004-1833). Intensity ratios of a reflection I_{hkl} to the sum $\Sigma I = I_{111} + I_{220} + I_{311}$ were calculated. I_{hkl} includes also contributions from all subreflection ascribed to PFs. These $I_{hkl}/\Sigma I$ ratios were normalized to what is expected from the random orientation given by the powder standard (i.e., $I_{111}/\Sigma I = 0.54$, $I_{220}/\Sigma I = 0.27$, $I_{311}/\Sigma I = 0.20$).

2.3 Electron microscopy

Conventional cross-sections were prepared by mechanical polishing followed by argon-ion milling at low-angle (Gatan PIPS). Specimens are thinned down to approximately 100 nm thickness. For As-implanted material and material annealed at 700 °C, TEM was carried out with an electron microscope (JEOL JEM-2010) equipped with a 200 kV field emission gun. For material annealed at 500 °C, the electron microscopy data acquisition was performed using a FEI Titan microscope (FEI Company, Eindhoven, the Netherlands), equipped with a CEOS image corrector (CEOS GmbH, Heidelberg, Germany), operated at 300 kV. For HR-TEM micrograph acquisition, the information limit of the microscope was tuned to 0.8 Å. For nanobeam electron diffraction measurements, the microscope was operated in STEM mode with a probe convergence angle of 1 mrad, resulting in an approximate beam size of 2–3 nm. Diffraction patterns were recorded in an array of points; each pattern was recorded with an exposure time of 100 ms with a beam current of <30 pA.

3 Results and discussion

3.1 An amorphous-to-crystalline transformation

Figure 1(a) shows a typical X-ray diffractogram recorded on InGaAsP/InP heterostructures after implantation with Fe ions. Two strong diffraction peaks are assigned to symmetrical (200) and (400) reflections from the single-crystal InP substrate. Two broad shapes, centered at $2\theta = 27°$ and 47° and a weaker and broader feature centered at 75°–80°, are also detected. Their angular location corresponds to reciprocal lengths of 0.30, 0.52, and 0.79 Å^{-1}. These shapes are ascribed to an implant-amorphized InGaAsP/InP layer, as XRD from amorphous materials produces a series of broad diffuse halos [16, 17]. The diffraction angles corresponding to these halos' locations are consistent with published values of similar amorphous semiconductors [18, 19]. With careful analysis of the shape of the scattered X-ray intensity, one can estimate the radial distribution of nearest atom neighbors of the amorphous solid [16, 17]. The formation of a thick amorphous layer is confirmed by TEM imaging (see Fig. S1 in the Supporting Information, online at: www.pss-a.com).

The layer extends through the heterostructure from the sample surface to an amorphous/crystalline interface located in the InP substrate about 0.3 μm below the InGaAsP layer.

Figure 1(b) shows a typical diffraction spectrum after further processing with RTA. The broad halos related to the implanted amorphous layer (at 27°, 47°, and 75°) are suppressed while the (200) and (400) substrate peaks are still present. In addition, a series of new peaks from a polycrystalline phase appear, these being located at diffracting angles corresponding to those of the cubic zincblende structure with the InP lattice parameter (5.87 Å). All reflections of the zincblende phase were observed. Signals related to (222) and (420) reflections are barely distinguishable from the background as they are the weakest peaks found in the InP powder diffraction standard. Symmetrical reflections (200) and (400) are hidden by substrate peaks.

The amorphous-to-crystalline transformation was studied by collecting XRD spectra taken for amorphous-like material and for material recrystallized with various RTA temperatures (see Fig. S2, Supporting Information). These XRD spectra were then reproduced by curve fitting [20]. Details of the fitting are given in Supporting Information. Structural parameters were extracted from the fitting results and are reviewed over the course of this paper. By analyzing integrated peak intensities, we can demonstrate that the polycrystalline InGaAsP/InP structure developed a small ⟨110⟩ preferential orientation of its coherent domains with diffracting planes perpendicular to the surface normal. This result is shown in Fig. 1(c). The preferential orientation does not vary much over the range of RTA temperatures. We also worked under the assumption that scattered intensities from both a residual amorphous phase (I_a) and a crystalline phase (I_c) can be present in the signal. Figure 1(d) shows I_a and I_c as a function of the RTA process temperature. According to Fig. 1(d) and (e), the crystalline volume fraction (X_c) in the InGaAsP/InP layers is significant. At an annealing temperature of 300 °C, X_c was ~0.84. The crystalline volume fraction appears unaffected by higher RTA temperatures which may suggest a mostly complete transformation. These observations are consistent with amorphous-to-crystalline transformations that are known to occur at even lower temperatures for InP: the onset of the transformation is observed at ~220 °C after few hours-long isochronal annealing cycles [21]. The exact fraction of the small residual amorphous phase signature remains difficult to quantify as our estimates likely include unassigned contributions from peak tails of symmetrical reflections and from other sources of diffuse scattering related to alloy imperfections.

3.2 A multilayered microstructure after recrystallization

TEM techniques can provide precise information on the spatial distribution and defects of the recrystallized phase found in Fe-implanted InGaAsP/InP after RTA. Figure 2(a) shows a cross-section view obtained with annular dark field scanning TEM (ADF-STEM) of material annealed at 500 °C. Figure 2(b) shows a cross-section view obtained with conventional TEM of material annealed at 700 °C.

Image contrast in both specimens of Fig. 2 shows multiple and distinct structural layers which are described next, from top to bottom. Large crystalline regions, sometimes extending over hundreds of nanometers, are found distributed throughout the InGaAsP layers. Many regions have an apparent (projected) elongation along one axis. Selected area electron diffraction (SAED) patterns taken across these InGaAsP layers indicate the presence of crystalline grains with large misorientation, as diffracted spots and streaks appear within discontinuous rings. The radial positions of these rings correspond to the interplanar *d*-spacings of a cubic zincblende structure lattice-matched to InP, consistent with XRD data. Distinct intensity maxima, observed on SAED rings, indicate some amount of preferred orientation of the recrystallization. Variations in the local grain structure are also found when sampling multiple SAED patterns on smaller adjacent areas of these polycrystalline InGaAsP layers. We detail such effects in Fig. S4 of the Supporting Information for the specimen recrystallized at 700 °C.

Two characteristic bands, although much thinner than the polycrystalline InGaAsP layer, are also clearly visible in Fig. 2. Just underneath the InGaAsP layer below I1, a defective band, finely streaked, causes intense diffuse scattering on the STEM micrograph (Fig. 2a) and shows as a dark band of streaked InP regions on the conventional TEM image (Fig. 2b). The orientation of the diffuse streaking associated with this structural band was determined with SAED and with nanobeam electron diffraction (NBED) mapping (see Figs. S5 and S6 of the Supporting Information). Diffraction patterns taken from this band are streaked along <111> and correspond to PF bundles growing epitaxially from I2, the former amorphous/crystalline (*a*/*c*) interface. Such observation of solid phase epitaxy with strong {111} planar disorder has been reported before [22–28]. Along with imaging and NBED, many oriented PF bundles remain confined to the InP, extending for less than 0.3 μm above the former a/c interface. Some twins are detected in the transition of the InP oriented PF band to the polycrystalline InGaAsP layer. A second band scattered with small contrasting dots is also visible from Fig. 2, below the PF band. This band encloses secondary defects associated with the “end-of-range” (EOR) damage, and extends for about 0.15 μm deeper into the substrate. These defects correspond to amorphous and defective clusters, formed by primary Fe ion damage at the EOR of the most energetic ions. For InP-related materials, these clusters typically produce dislocation loops as they annealed out [29]. One EOR defect has been imaged by HR-TEM on the 700 °C specimen. A coffee-bean shape of its TEM contrast was detected, typical of dislocation loops and coherent precipitates [30].

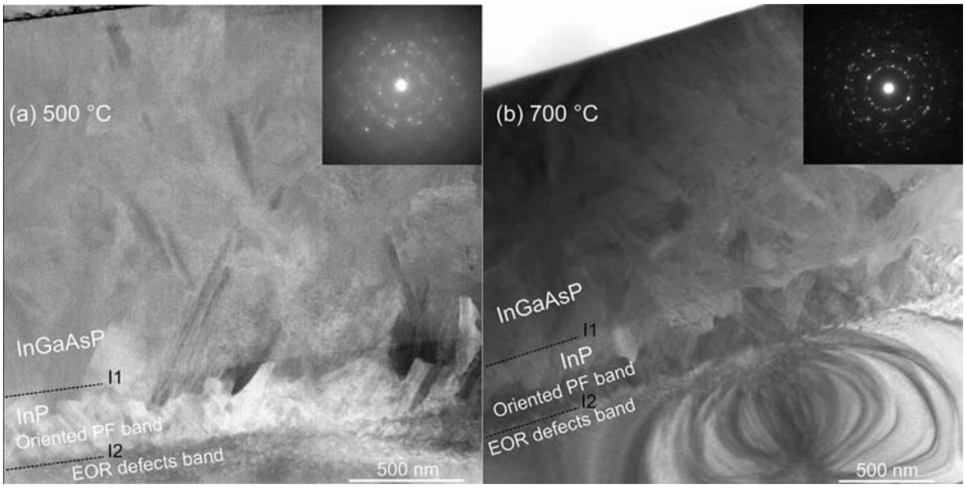

Figure 2 (a) ADF STEM micrograph taken on a cold Fe-implanted InGaAsP/InP heterostructure annealed at 500 °C. (b) TEM micrograph taken on another heterostructure annealed at 700 °C. The electron beam is at the [011] zone axis of the substrate, showing bend contours. For both micrographs, dotted lines I1 indicate the interface between InGaAsP and InP materials. Dense bundles of oriented planar faults (PF) and EOR defects can be observed near dotted lines I2, the former *a*/*c* interface. Insets are showing typical SAED patterns taken across the polycrystalline InGaAsP layers.

3.3 The nanoscale substructure of the polycrystalline InGaAsP layer The TEM specimen shown in Fig. 2(a) was thinned further to produce detailed microstructural images of the polycrystalline InGaAsP layer. We selected this specimen because desirable optoelectronic properties, such as ultrafast photocarrier dynamics and high dark resistivity, are achieved after recrystallization at 500 °C. At lower TEM magnification, the image of Fig. 3(a) shows the streaked substructure of three InGaAsP grains. At high resolution in Fig. 3(b), (111) lattice fringes are clearly visible. Their real-space average *d*-spacing is 0.341(5) nm. The (111) fringe contrast of G1 is often striated, finer at grain periphery, and runs parallel (or almost parallel) to (111) planes.

Such intragrain contrast reveals a high density of (111) planar defects, local strain from dislocations, and crystallographic texture. Grain G1 contains oriented lamellar regions in its interior, some are designated by L on the

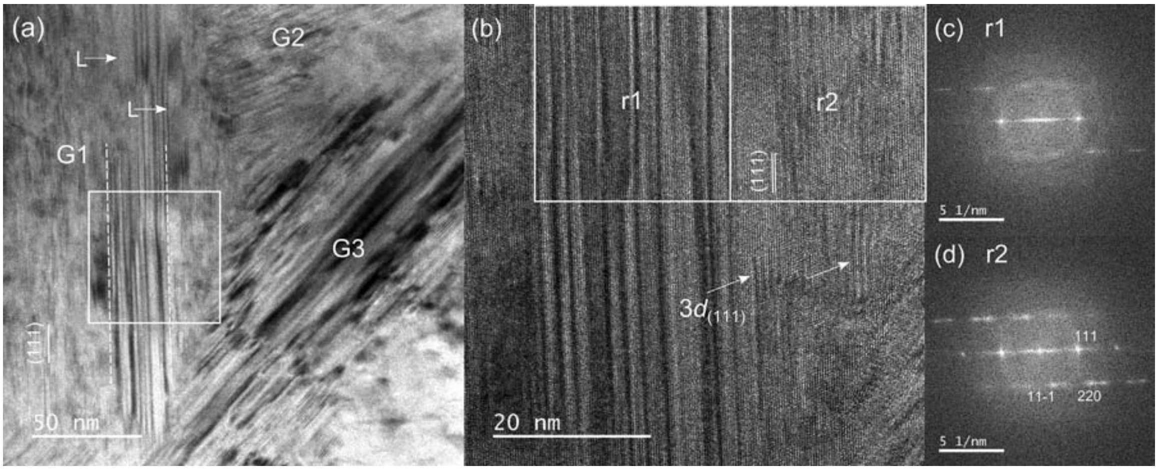

Figure 3 (a) TEM cross-section image from the top part of the InGaAsP layer recrystallized at 500 °C. The image contrast of grains, labelled G1, G2, and G3, make striations running at different angles. In a band in the middle of G1, delimited by two dashed lines, the contrast is coarser and runs rather continuously. In G1, thin lamellae (L) extending vertically are indicated by arrows. In G3, the contrast is stronger and complex, sometimes stopping abruptly. (b) HR-TEM close-up corresponding to a region delimited by a square in (a). (111) lattice fringes are observed. Fine details of the contrast are highlighted in regions labelled r1 (coarser bands) and r2 (finer bands) for which Fourier transforms are given in (c) and (d) and showing diffuse scattering and streaking. Below r2, arrows indicate local variation of the contrast as a modulation of the (111) lattices fringes with a period of $3d_{(111)}$.

image. They are bounded at (111) planes and their widest thicknesses are about 5–8 nm. The lamellar elongation is directed toward <211>. For solid phase recrystallization, exaggerated growth along this axis is consistent with faulting on (111) planes in case of twinning [31]. At the periphery of grain G1, a modulation of the (111) lattice contrast at a triple-period is observed in small regions, 7–10 nm wide, below r2 in Fig. 3(b). This irregularity may correspond to Moiré patterns resulting from the superposition of small coherent (111) twin subdomains [32]. A fine striated contrast is also observed in region r2; however, it is not as clear and periodic, perhaps due to local strain fields or mutual misorientation. A small anisotropy of *d*-spacings can be detected on the Fourier transformed (FT) image of r2 (Fig. 3d). One set (−111) appears expanded by about 5% compared to the other one (111) which is closer to an unstrained lattice. Since microscope astigmatism is removed in the alignment procedure, such possibility can be ruled out. This anisotropy of the FT/HR-TEM pattern remains not satisfactorily explained and requires further investigation.

3.4 Correlating TEM results and XRD peak shape analysis XRD peak shapes correlate in many ways to the nanoscale substructure of the InGaAsP submicron grains. In Fig. 4(a), we show the evolution of the (111) Bragg reflection with various RTA temperatures. The base of the (111) reflections is made of a broad composite peak. The shoulder at the low angle side can be attributed to the dilatation of (111) interplane spacings at coherent domain boundaries [33]. This typical peak shape is often found in face-centered cubic, diamond, and zincblende crystals that are structurally faulted along close-packed {111} lattice planes [34–36]. Since planar faults modify the order of the atom stacking sequence, structurally faulted cubic crystals can locally appear as a polytypic hexagonal phase in the XRD diffractogram [14].

The diffraction angle of the peak needed to reproduce the low-angle shoulder of the (111) reflection in our recrystallized InGaAsP samples is compatible with the strongest diffraction peak calculated for wurtzite InP [37]. Such closed-packed $(10\bar{1}0)$ planes, with interplanar spacings of 3.578 Å, diffract at a Bragg angle of $2\theta = 24.9°$. This agreement can be seen in Fig. S3(b) (see Supporting Information). Also noticeable in Fig. S3(b) are XRD peak shapes corresponding to ‘Super-Lorentzian’ line profiles, i.e., with tails falling off more slowly than for a Lorentzian. These peaks are rather symmetric. ‘Super-Lorentzian’ profiles are often observed with faulted structures, in which cases twin faults happen to cause symmetric tails [36, 38]. Using fit parameters found for the (111) reflection, the ratio of the intensity of the broad composite peak attributed to PFs $(I^{\text{p.f.}}_{111})$ relative to the total peak intensity (I_{111}) was calculated [39].

The result is shown in Fig. 4(b) at various RTA temperatures. The ratio is maximum and almost constant for RTA plateau temperatures below 500 °C. This suggests that PFs are formed at low temperatures with a high fault probability in the polycrystalline phase, including temperatures corresponding to the heating up of the sample. The ratio then decreases appreciably at higher temperatures. Apparently, a minimum RTA plateau temperature is necessary to significantly anneal out PFs.

XRD peak shapes are also influenced by the size and shape of regions over which diffraction is coherent. Grain boundaries and planar defects limit such coherent lengths and cause peak broadening. From the full-width at half-maximum (B_{hkl}) of each diffraction peak, we made estimates of the apparent size of the coherent domain population (i.e., a volume-weighted mean size). We use the set of sharp lines (as described in the Supporting Information) which contains information on domain sizes. For Lorentzian line profiles, the experimental peak width (reproduced by fitting) can be written as follows:

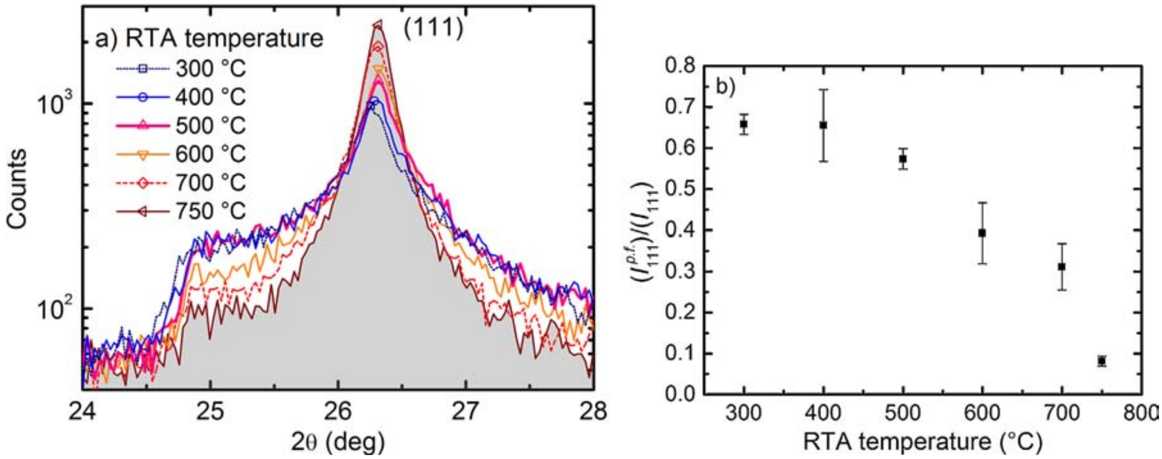

Figure 4 (a) Details of the (111) XRD reflection of Fe-implanted InGaAsP/InP samples recrystallized at different RTA temperatures. (b) Intensity of the (111) signal associated with planar faults relative to the total diffracted intensity at different RTA plateau temperatures.

$B_{\mathrm{exp}} = B_{hkl} + B_{\mathrm{ins}}$, where B_{ins} is the instrument's broadening function. We show *hkl* peak broadening in a Williamson–Hall (W–H) representation. Peak widths in the reciprocal space $B^*_{hkl} = B_{hkl}(2\theta) \cdot \cos(\theta)/\lambda$ are plotted against $d^* = 2\sin\theta/\lambda$, the inverse lattice plane spacing at the Bragg angle. In a W–H representation, B^*_{hkl} is constant with d^* for isotropic size effects only (i.e., the Scherrer equation). A slope often implies microscopic strain gradients. In general cases, size is given by the intercept [40]. Peak widths collected in the course of this work at $d^* > 6\,\mathrm{nm}^{-1}$ were also taken into account for a meaningful W–H analysis, shown in Fig. 5.

The W–H plot shows a general increasing trend of B^*_{hkl} with d^*. However, this trend is not linear and not monotonous. Linear fitting of pair of data points that are related to higher order reflections (i.e., (220) and (440) for material annealed at 500 and 550 °C) yields to a small negative intercept. In that case, anisotropic microstrain-like broadening due to dislocations, anisotropic domain shapes, or effects resulting from the interference between mutually coherent diffracting domains have to be considered [41]. A strong local preferred orientation is prerequisite for visible partial mutual coherence effects on diffraction line broadening of nanocrystalline materials [42, 43]. For low d^*, nanoscale regions of the recrystallized grains could diffract coherently, giving rise to a narrowing of the diffraction peaks in Fig. 5. As d^* increases, a gradual loss of partial coherence between nanoscale regions explains the upward curvature of the line broadening. An abrupt and plateau-like change in B^*_{hkl} is observed above $d^* = 6\,\mathrm{nm}^{-1}$ for two samples annealed at 500 and 550 °C and corresponds to an incoherent diffraction regime. This plateau-like broadening corresponds to a mean apparent size $K/\langle B^*_{hkl}\rangle$ of $10 \pm 0.5\,\mathrm{nm}$. A default value of the Scherrer constant $K = 0.9$ was used as a first approximation [44]. One cannot forget that such basic size estimate associated with XRD peak broadening is a sum of size and shape effects from a very heterogeneous material. Some regions have faults, small grains, others do not. However, when taking into account a partial coherence effect, the XRD size estimate is in relatively good agreement with our TEM observations of internally faulted grain substructures, showing TEM contrasted regions of comparable sizes. Furthermore, one can notice in Fig. 5 that the peak broadening of (331) is particularly influenced by the RTA temperature. According to the interpretation of the W–H plot discussed hereabove, diffracted signals are adding up incoherently for (331). The RTA temperature appears then to have an influence on the sizes and shapes of nanoscale regions or, in other terms, on the intragrain defect distributions.

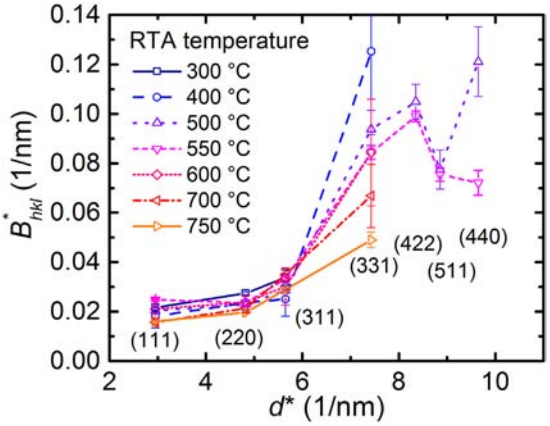

Figure 5 W–H representation of the *hkl* broadening from XRD peaks. Peak widths (in reciprocal space) are obtained for different annealing temperatures of the recrystallized Fe-implanted InGaAsP material.

4 Discussion on recrystallization and "macroscopic" optoelectronic properties

The present work introduced XRD techniques, paired with electron microscopy, to study structural defects developing at various RTA conditions of the recrystallization of Fe-implanted InGaAsP/InP heterostructures. The cumulative damage of the cold Fe ion implantation sequence induced an amorphous transition through the thick InGaAsP layer and the top part of the InP wafer. This created particular initial conditions to the recrystallization, in addition to the incorporation of excess Fe impurities at about $1 \times 10^{19}\,\mathrm{cm}^{-3}$, much greater than the normally believed solid solubility limit of Fe in InP-related alloys (10^{17}–$10^{18}\,\mathrm{cm}^{-3}$) [29, 45]. Some of the complexities of the RTA-induced recrystallization resulted from the interplay of two growth mechanisms: solid phase epitaxy occurring from the a/c interface and solid phase recrystallization happening into the InGaAsP layer, the latter being responsible for the polycrystalline structure. Clustering of excess Fe impurities appears probable; however, our attempts to detect Fe-rich nanoscale clusters by EELS were not successful due to small Fe concentration levels and the thickness of our cross-section specimens. In addition, substantial faulting and associated dislocations are suspected to help accommodating for Fe impurities above their solid solubility limit in the recrystallized InGaAsP layer [46]. Polycrystalline recrystallizations of binary III–V compounds had previously been identified by TEM in MeV ion implantation works. Auvray et al. found a thin polycrystalline phase close to sample surfaces after 800 keV Se implantation done at room temperature in InP [22]. Polycrystalline layers formed in the central part between two a/c interfaces were also reported by Narayanan and Spitzer for 2.7 MeV P implantation in GaAs [47], by Xiong et al. for 15 MeV N implantation in InP [48], and by Jasinski et al. for 2 MeV As or Ga ion implantation in GaAs [27].

In the context of pulsed photoconductive terahertz applications, control over the recrystallization of the amorphous InGaAsP/InP heterostructure, and its outcomes, is essential for refining macroscopic optoelectronic properties of the material. For instance, a maximization of the on-chip dark resistivity is obtained in heterostructures recrystallized at moderate RTA temperatures, around

500 °C [3]. Since carrier transport properties may vary within the defective layers of the InGaAsP/InP microstructure, possibilities for parallel conduction need to be examined further to better explain the workings of this optimization. Concerning photocarrier dynamics, the material demonstrates fast exponentially decaying signals in pump–probe photoreflection and phototransmission measurements [3, 11]. Sub-picosecond decay times, less than 0.7 ps, are observed when the RTA temperature is moderate (500 °C or below). Above 500 °C, significantly longer decays are measured in the photoreflection response [3]. Structurally, the relative diffracted intensity ascribed to PFs decreases significantly above 500 °C in Fig. 3. Progressive increases in the apparent size of XRD-coherent domains are also observed with RTA temperatures in Fig. 5. This appears consistent with previous observations made on microcrystalline Si by time-resolved terahertz spectroscopy, linking rapid photocarrier dynamics to the nanoscale size of crystalline domains, and the nature of their boundaries [49]. Typically, submicron polycrystalline columnar growth and nanoscale twinning are found in microcrystalline Si layers [13, 34]. The defect structures of the submicron grained polycrystalline InGaAsP:Fe layers are, however, more complex and heterogeneous. PFs are generally considered as electronically inactive [50], but electronic states associated with dangling bonds found at their edges, at partial dislocation cores, or associated with Fe impurity atoms “contaminating” partial dislocations or fault planes may influence the photocarrier capture rates [51, 52]. As the occurrence of PFs in the (111) stacking sequence of zincblende crystals happens to form small band alignment discontinuities [53], further examinations are also needed to determine whether microscopic carrier scattering effects at small intragrain potential barriers are significant to the material’s photocarrier dynamics.

5 Conclusions With a post-growth process such as Fe ion implantation and rapid thermal annealing, one can modify a single layer bulk InGaAsP/InP heterostructure into a complex nanostructured material that is promising for the development of ultrafast optoelectronic switching and photomixing devices. This paper brings forward additional connections to be made between microstructural parameters and functional properties of this material that are RTA-temperature dependent. Given the probable importance of Fe atom redistribution, crystalline domain sizes, and PF configurations on photoconductive properties of Fe-implanted InGaAsP layers, a finer control of the recrystallization’s temperature–time profile can be envisioned to refine device performances, a work that can be assisted by nondestructive XRD characterization and verified by electron microcopy techniques.

Supporting Information

Additional supporting information may be found in the online version of this article at the publisher’s website.

Acknowledgements We would like to thank S. Gutierrez, material analyst at the Centre de Caractérisation des Matériaux—CCM (Université de Sherbrooke) for conducting powder XRD measurements and Dr. J. P. Masse, microscopist at the Centre de Caractérisation Microscopique des Matériaux—(CM)^2 (École Polytechnique de Montréal) for conducting TEM observations. Some of the electron microscopy work presented here were carried out at the Canadian Centre for Electron Microscopy (CCEM), a national facility supported by McMaster University and NSERC. Stimulating discussions and suggestions to the paper from Prof. G. Botton, of McMaster University, are gratefully acknowledged. We also wish to thank Dr. S. Schicho and Prof. N. Braidy of Université de Sherbrooke for useful conversations on XRD and TEM. The project was supported by Fonds Québecois sur la Nature et les Technologies and by NanoQuébec.

References

[1] C. Carmody, H. H. Tan, C. Jagadish, A. Gaarder, and S. Marcinkevicius, Appl. Phys. Lett. **82**(22), 3913 (2003).

[2] J. H. Shin, K. H. Park, N. Kim, C. W. Lee, E. D. Shim, Y. C. Kim, D. S. Yee, J. O. Kim, S. J. Lee, and S. K. Noh, AIP Conf. Proc. **1399**(1), 935 (2011).

[3] A. Fekecs, M. Bernier, D. Morris, M. Chicoine, F. Schiettekatte, P. Charette, and R. Arès, Opt. Mater. Express **1**(7), 1165 (2011).

[4] M. Suzuki and M. Tonouchi, Appl. Phys. Lett. **86**(5), 51104 (2005).

[5] M. Suzuki and M. Tonouchi, Appl. Phys. Lett. **86**(16), 163504 (2005).

[6] J. Lloyd-Hughes, E. Castro-Camus, M. D. Fraser, H. H. Tan, C. Jagadish, and M. B. Johnston, Proc. SPIE **6118**, 61180K (2006).

[7] J. Shin, N. Kim, W. L. Chul, E. Sim, H. P. Kyung, Dae-Su Yee, Y. J. Min, J. O. Kim, Y. Jang, Y. Kim, J. L. Sang, and K. N. Sam, 34th International Conference on Infrared, Millimeter, and Terahertz Waves (IRMMW-THz), IEEE, 2009, doi: 10.1109/ICIMW.2009.5325661.

[8] M. Tani, K. Yamamoto, E. S. Estacio, C. T. Que, H. Nakajima, M. Hibi, F. Miyamaru, S. Nishizawa, and M. Hangyo, J. Infrared Millimeter Terahertz Waves **33**(4), 393 (2012).

[9] M. Xu, M. Mittendorff, R. J. B. Dietz, H. Künzel, B. Sartorius, T. Göbel, H. Schneider, M. Helm, and S. Winnerl, Appl. Phys. Lett. **103**(25), 251114 (2013).

[10] H. H. Tan, C. Jagadish, M. J. Lederer, B. Luther-Davies, J. Zou, D. J. H. Cockayne, M. Haimi, U. Siegner, and U. Keller, Appl. Phys. Lett. **75**(10), 1437 (1999).

[11] M. Martin, E. R. Brown, J. Mangeney, A. Fekecs, R. Arès, and D. Morris, in: 37th International Conference on Infrared, Milimeter, and Terahertz Waves (IRMMW-THz), IEEE, 2012, doi: 10.1109/IRMMW-THz.2012.6380277.

[12] J.-L. Coutaz Acta Phys. Pol. A **102**(4–5), 495 (2002).

[13] L. Houben, M. Luysberg, P. Hapke, R. Carius, F. Finger, and H. Wagner, Philos. Mag. A **77**(6), 1147 (1998).

[14] S. Schicho, F. Kohler, R. Carius, and A. Gordijn, Sol. Energy Mater. Sol. Cells **98**, 391 (2012).

[15] S. Schicho Ph.D Thesis, Forschungszentrum Jülich GmbH (2011).

[16] H. P. Klug and L. E. Alexander, X-ray Diffraction Procedures: For Polycrystalline and Amorphous Materials, 2nd edn. (Wiley-VCH, New York, 1974).

[17] A. Guinier, X-ray Diffraction, in: Crystals, Imperfect Crystals, and Amorphous Bodies, 2nd edn. (Dover Publications, New York, 1994).

[18] S. C. Moss and J. F. Graczyk, Phys. Rev. Lett. **23**(20), 1167 (1969).

[19] M. H. Brodsky, R. S. Title, K. Weiser, and G. D. Pettit, Phys. Rev. B **1**(6), 2632 (1970).

[20] M. Wojdyr J. Appl. Cryst. **43**(5), 1126 (2010).

[21] G. de M. Azevedo, C. J. Glover, M. C. Ridgway, K. M. Yu, and G. J. Foran, Phys. Rev. B **68**(11), 115204 (2003).

[22] P. Auvray, A. Guivarc'h, H. L'Haridon, G. Pelous, M. Salvi, and P. Henoc, J. Appl. Phys. **53**(9), 6202 (1982).

[23] C. Licoppe, Y. I. Nissim, C. Meriadec, and P. Henoc, Appl. Phys. Lett. **50**(23), 1648 (1987).

[24] M. C. Ridgway, G. R. Palmer, R. G. Elliman, J. A. Davies, and J. S. Williams, Appl. Phys. Lett. **58**(5), 487 (1991).

[25] P. Mueller, W. Wesch, V. S. Solovyev, P. I. Gaiduk, E. Wendler, F. F. Komarov, and G. Goetz, Nucl. Instrum. Methods B **80–81**, 721 (1993).

[26] K. B. Belay, D. J. Llewellyn, and M. C. Ridgway, Appl. Phys. Lett. **69**(15), 2255 (1996).

[27] J. Jasinski, Z. Liliental-Weber, J. Washburn, H. H. Tan, C. Jagadish, A. Krotkus, S. Marcinkevicius, and M. Kaminska, J. Electron Mater. **26**(5), 449 (1997).

[28] C. Frigeri, A. Carnera, B. Fraboni, A. Gasparotto, A. Cassa, F. Priolo, A. Camporese, and G. Rossetto, Mater. Sci. Eng. B B **44**(1–3), 193 (1997).

[29] A. Gasparotto, A. Carnera, C. Frigeri, F. Priolo, B. Fraboni, A. Camporese, and G. Rossetto, J. Appl. Phys. **85**(2), 753 (1999).

[30] D. B. Williams and C. B. Carter, Transmission Electron Microscopy, A Textbook for Materials Science, 2nd edn. (Springer, New York, 2009).

[31] C. Spinella, S. Lombardo, and F. Priolo, J. Appl. Phys. **84**(10), 5383 (1998).

[32] L. Haji, P. Joubert, J. Stoemenos, and N. A. Economou, J. Appl. Phys. **75**(8), 3944 (1994).

[33] S. Veprek, F. A. Sarott, and Z. Iqbal, Phys. Rev. B **36**(6), 3344 (1987).

[34] L. Houben, M. Luysberg, and R. Carius, Phys. Rev. B **67**(4), 45312 (2003).

[35] F. Köhler, T. Chen, M. Nuys, A. Heidt, M. Luysberg, F. Finger, and R. Carius, J. Non-Cryst. Solids **358**(17), 2011 (2012).

[36] L. Balogh, G. Ribárik, and T. Ungár, J. Appl. Phys. **100**(2), 023512 (2006).

[37] P. I. Gaiduk, F. F. Komarov, V. S. Tishkov, W. Wesch, and E. Wendler, Phys. Rev. B **61**(23), 15785 (2000).

[38] E. Estevez-Rams, A. Penton, J. Martinez-Garcia, and H. Fuess, Cryst. Res. Technol. **40**(1–2), 166 (2005).

[39] F. Köhler, T. Chen, C. Sellmer, T. Bronger, A. Heidt, F. Finger, and R. Carius, in: 25th International Conference on Amorphous and Nano-Crystalline Semiconductors, Toronto, Canada, August 2013.

[40] B. D. Cullity and S. R. Stock, Elements of X-ray Diffraction, 3rd edn. (Prentice-Hall, Upper Saddle River, NJ, 2001).

[41] E. J. Mittemeijer and U. Welzel, Z. Kristallogr. **223**(9), 552 (2008).

[42] D. Rafaja, V. Klemm, G. Schreiber, M. Knapp, and R. Kuzel, J. Appl. Cryst. **37**(4), 613 (2004).

[43] L. Gelisio and P. Scardi, J. Nanosci. Nanotechnol. **12**(11), 8811 (2012).

[44] J. I. Langford and A. J. C. Wilson, J. Appl. Cryst. **11**, 102 (1978).

[45] J. Vellanki, R. K. Nadella, M. Rao, O. W. Holland, D. S. Simons, and P. H. Chi, J. Appl. Phys. **73**(3), 1126 (1993).

[46] D. K. Sadana Nucl. Instrum. Methods B **7–8**(1), 375 (1985).

[47] G. H. Narayanan and W. G. Spitzer, J. Mater. Sci. **13**(11), 2418 (1978).

[48] F. Xiong, C. W. Nieh, and T. A. Tombrello, Ultramicroscopy **30**(1–2), 242 (1989).

[49] L. Fekete, P. Kuzel, H. Nemec, F. Kadlec, A. Dejneka, J. Stuchlik, and A. Fejfar, Phys. Rev. B **79**(11), 115306 (2009).

[50] S. Mahajan Acta Mater. **48**(1), 137 (2000).

[51] X. Xu, S. P. Beckman, P. Specht, E. R. Weber, D. C. Chrzan, R. P. Erni, I. Arslan, N. Browning, A. Bleloch, and C. Kisielowski, Phys. Rev. Lett. **95**(14), 145501 (2005).

[52] B. Chen, J. Chen, T. Sekiguchi, M. Saito, and K. Kimoto, J. Appl. Phys. **105**(11), 113502 (2009).

[53] A. Belabbes, C. Panse, J. Furthmuller, and F. Bechstedt, Phys. Rev. B **86**(7), 075208 (2012).